International Journal of Non-Linear Mechanics 46 (2011) 415–424

Contents lists available at ScienceDirect

International Journal of Non-Linear Mechanics

journal homepage: www.elsevier.com/locate/nlm

Non-linear suspension of an automatic ball balancer

T.C. Chan [a,c], C.K. Sung [a,*], Paul C.P. Chao [b]

[a] Department of Power Mechanical Engineering, National Tsing Hua University, Hsinchu 30013, Taiwan, R.O.C
[b] Department of Electrical Engineering, National Chiao Tung University, Hsinchu 30013, Taiwan, R.O.C
[c] Precision Machinery Research and Development Center, Taichung 40768, Taiwan, R.O.C

ARTICLE INFO

Article history:
Received 10 April 2010
Received in revised form
20 July 2010
Accepted 1 November 2010
Available online 10 November 2010

Keywords:
Automatic ball balancer
Non-linear suspension
Residual vibration

ABSTRACT

This study investigates the effects on ball positioning because of the non-linear suspensions of an automatic ball balancer (ABB) installed in a rotor system. A complete dynamic model of the ABB, focusing on the non-linearity of the suspensions, is presented. The elastic behaviour of these suspensions is assumed to be well characterised by equivalent non-linear springs. Herein, two Duffing-type non-linear springs are considered: stiffness-softening and stiffness-hardening. Four types of asymptotic solutions that represent the ball positions at steady state are obtained by employing the method of multiple scales. The stabilities of all four types of solutions were found using Floquet theory. In contrast to the perfectly balanced solutions (Type I), the other solution (Type II) is affected by non-linear stiffness suspension. After properly designing the avoidable level of non-linearity, the balancing balls of the ABB still resided at the positions required to reduce the expected vibrations in the steady state. Numerical simulations were performed to validate the theoretical results. The results were also used to predict the level of residual vibration, and design guidelines that would guarantee the desired performance of the ABB for high-precision applications were formulated.

1. Introduction

Imbalances are the standard cause of vibrations in high-speed rotating equipment. To offset rotor imbalance, off-line balancing methods are commonly used in industrial applications. However, if the imbalance varies during operation, it cannot be eliminated only by off-line balancing methods. The automatic ball balancer (ABB) is a typical example of a passive-type system. Although the ABB is effective in reducing vibrations, it still has consistency issues according to previous works. The ABB, which consists of free-running balls inside races, can almost completely eliminate radial vibrations via the concept of counterbalancing. This is based on the fact that as the spindle speed of a rotor exceeds the resonant frequency, the balls inside the race are driven to the opposite of the imbalance by the centrifugal and normal forces created by rotor rotation. Indeed, significant counterbalancing can be achieved via this mechanism.

Thearle [1,2] presented an early analysis of various types of balancing systems and found ball-type balancers to be superior to other types due to low friction, low cost, and ease of implementation. Majewski [3] found the negative effects of ball-rolling resistance, race eccentricity, and external vibrations on the rotor/balancer system at steady state. Rajalingham et al. [4] were the first to include the contact friction of the balancing balls in a model. Huang et al. [5] introduced a simple stick-slip model and illustrated the unavoidable rolling friction between the balancing balls and the race flange actually deterred the balls from residing precisely at the desired positions. Lu and Hung [6] explored a theoretical model with a three-ball ABB was constructed. Rodrigues et al. [7] presented an analysis of a two-plane ABB for rigid rotors. DeSmidt [8] developed the dynamics and stability of an imbalanced flexible shaft equipped with an ABB. Liu and Ishida [9] presented the vibration suppression method utilising the discontinuous spring characteristics together with an ABB. The non-linearity will influence the amplitude and the phase angle of vibration. Therefore, non-linearity is one of the key factors responsible for the inconsistency and ball mispositioning of an ABB. Ehyaei and Moghaddam [10] developed a system of unbalanced flexible rotating shafts equipped with n ABBs where the unbalanced masses were distributed along the length of the shafts. Green et al. [11] presented the non-linear bifurcation analysis of a two-ball automatic dynamic balancing mechanism for eccentric rotors.

These previous studies only adopted linear stiffness models for the suspension, neglecting the profound influence of suspension non-linearity. However, there is non-linearity in many mechanical systems and spring components. Chao et al. [12] was the first to explore the non-linear dynamic effects of damping washers on the performance of an ABB installed in optical disc drives.

This paper proposes a theoretical study of the effects of non-linear suspension on the ball positioning for an ABB. This non-linearity influences the amplitude and phase angle of suspension vibration, which is considered as one of the key factors that affect ball positioning when using an ABB. A complete dynamic model of

* Corresponding author. Tel.: +886 3 5742918; fax: +886 3 5715314.
E-mail addresses: d9533830@oz.nthu.edu.tw (T.C. Chan), cksung@pme.nthu.edu.tw (C.K. Sung), pchao@mail.nctu.edu.tw (P.C. Chao).

0020-7462/$ - see front matter
doi:10.1016/j.ijnonlinmec.2010.11.001

Nomenclature

G_R	Centre of gravity (C.G.) of the equivalent rotor
G_S	Centre of gravity of the equivalent stator
M_R	Mass of the equivalent rotor
M_S	Mass of the equivalent stator
O_B	Centre of a ball
O_S	Rotational centre of the rotor
O_R	Origin of the inertial coordinate
O_r	Centre of the circular runway of the balancer
ρ	Runway eccentricity
e	Imbalanced eccentricity
β	Lead angle for imbalance
ϕ_i	Lead angle of ball's positions
B_i	Number of balls
m	Ball mass
r	Ball radius
$K_X+\gamma_x X^3$	Non-linear stiffness in the X direction
$K_Y+\gamma_y Y^3$	Non-linear stiffness in the Y direction
C_x	Damping in the X direction
C_y	Damping in the Y direction
p	Speed ratio ω/ω_n
ε	Scaling parameter. $\sqrt{m/M}$.
ω_n	Natural frequency of the suspension
τ	Normalised time scale
R	Race radius
α_1	Adhesive coefficient
α_0	Rolling friction coefficient of the ball balancer
θ	Rotating angle of the disc

the ABB, focusing the non-linearity of the suspension on the ball positioning of the ABB, is proposed. The method of multiple scales was applied to find all possible steady-state ball positions and their stabilities. Based on theoretical results, the design guidelines for the implementation of an ABB were formulated.

2. Mathematical model

The amplitude and phase are key factors for ball positioning in an ABB. The physical system of the rotor and the ball balancer can be simplified as shown schematically in Fig. 1. The linear and non-linear response curves are shown in Fig. 2.

The equations of motion for the rotor system can then be derived as follows:

$$\begin{aligned} M\ddot{X}+C_x\dot{X}+K_xX+\gamma_xX^3 = {} & M_R[\rho\ddot{\theta}\sin\theta+\rho\dot{\theta}^2\cos\theta \\ & +e\ddot{\theta}\sin(\theta+\beta)+e\dot{\theta}^2\cos(\theta+\beta)] \\ & +m\sum_{i=1}^{n}[\rho\ddot{\theta}\sin\theta+\rho\dot{\theta}^2\cos\theta \\ & +R(\ddot{\theta}+\ddot{\phi}_i)\sin(\theta+\phi_i) \\ & +R(\dot{\theta}+\dot{\phi}_i)^2\cos(\theta+\phi_i)], \end{aligned} \tag{1}$$

$$\begin{aligned} M\ddot{Y}+C_y\dot{Y}+K_yY+\gamma_yY^3 = {} & M_R[-\rho\ddot{\theta}\cos\theta+\rho\dot{\theta}^2\sin\theta \\ & -e\ddot{\theta}\cos(\theta+\beta)+e\dot{\theta}^2\sin(\theta+\beta)] \\ & +m\sum_{i=1}^{n}[-\rho\ddot{\theta}\cos\theta+\rho\dot{\theta}^2\sin\theta \\ & -R(\ddot{\theta}+\ddot{\phi}_i)\cos(\theta+\phi_i) \\ & +R(\dot{\theta}+\dot{\phi}_i)^2\sin(\theta+\phi_i)], \end{aligned} \tag{2}$$

$$\begin{aligned} \left(m+\frac{I}{r^2}\right)R(\ddot{\phi}_i+\ddot{\theta}) = {} & m\big[(\ddot{X}-\rho\ddot{\theta}\sin\theta-\rho\dot{\theta}^2\cos\theta)\sin(\phi_i+\theta) \\ & -(\ddot{Y}+\rho\ddot{\theta}\cos\theta-\rho\dot{\theta}^2\sin\theta)\times\cos(\phi_i+\theta)\big]-\alpha_1R\dot{\phi}_i \\ & -\frac{M_f}{r}sign(\dot{\phi}_i)+\frac{(R+r)}{r^2}I\ddot{\theta} \quad i=1,2,3\ldots,n. \end{aligned} \tag{3}$$

where $M=M_R+M_S+nm$ with M_R,M_S, and m denoting the masses of the equivalent rotor, stator, and ball, respectively. n denotes the number of balls. The terms γ_xX^3 and γ_yY^3 are the first non-linear stiffness terms of the suspensions in the X and Y directions, respectively.

3. Asymptotic analysis

Approximate solutions are sought by assuming some scalings to manipulate the equations of motion (1)–(3) and by applying

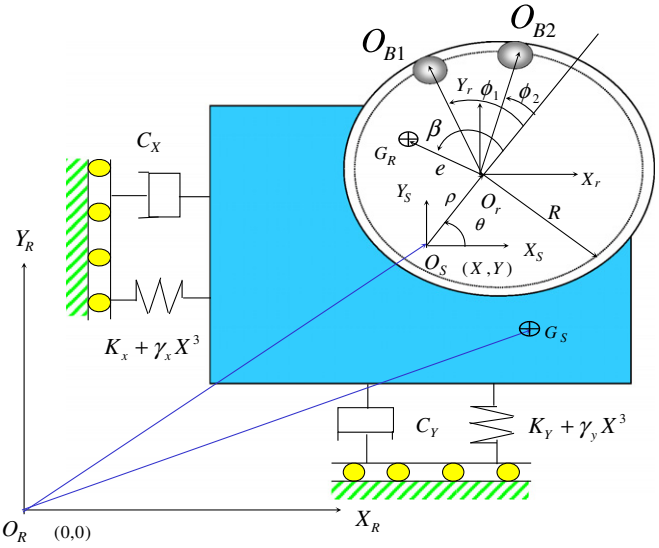

Fig. 1. Mathematical model of an automatic ball balancer with non-linear suspensions.

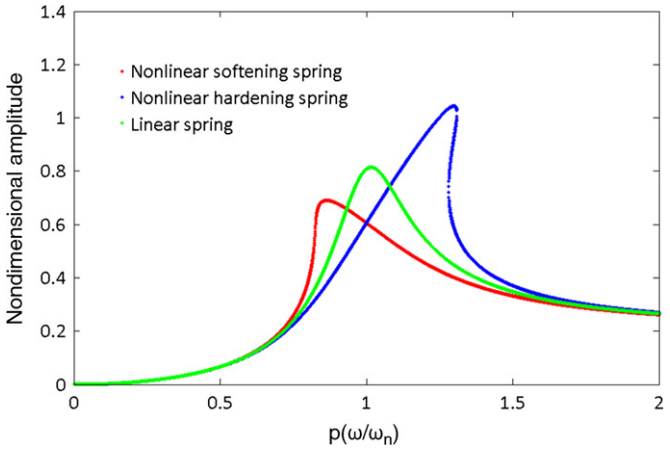

Fig. 2. Comparison of linear and non-linear response curves with respect to amplitudes.

techniques of asymptotic multiple-scale analysis

$$\varepsilon=\sqrt{m/M},\quad \omega_n=\sqrt{K/M},\quad \varepsilon x=X/R,\quad \varepsilon y=Y/R,$$
$$p=\omega/\omega_n,\quad \tau=\omega_n t,\quad \varepsilon^2\lambda_1=\rho/R,\quad \varepsilon^2\lambda_2=e/R,$$
$$\varepsilon\zeta_1=\alpha_1/m\omega_n,\quad \mu=m/(m+I/r^2),\quad \varepsilon\zeta=C/M\omega_n,$$
$$\varepsilon\zeta_0=\alpha_0/r,\quad \alpha=M_R/M,\quad \varepsilon\xi_2=\gamma_x R^2/M{\omega_n}^2=\gamma_y R^2/M{\omega_n}^2,$$
$$\varepsilon\lambda=(r+R)I/mr^2R, \tag{4}$$

where the small parameter ε serves as a small scaling parameter, while τ is a normalised time scale. Substituting Eq. (4) into the system equations of motion (1)–(3) and considering the case of two balls, i.e., $n=2$, and a constant rotating speed at a steady state near the linear resonance. Note that $\ddot{\theta}=0,\quad \dot{\theta}=p,\quad \theta=p\tau$. To facilitate ensuing asymptotic analysis, the square of the speed ratio p is represented by $p^2=1+\varepsilon\sigma$, where σ captures the scaled deviation of p^2 from one. Note that the scaling $p^2=1+\varepsilon\sigma$ implies that the analysis in the paper is only valid near the natural frequency of the system. However, since no super or sub-harmonic resonance is present due to weak excitation as shown in the equations, the approximate solutions could be able to predict the dynamics away from the primary resonance. Then, we obtain

$$\begin{aligned}
\ddot{x}+p^2x&=\varepsilon\{-\xi_2x^3-\zeta\dot{x}+\sigma x+\alpha p^2[\lambda_1\cos p\tau+\lambda_2\cos(p\tau+\beta)]\\
&\quad+2\varepsilon^2\lambda_1p^2\cos p\tau+\ddot{\phi}_1\sin(p\tau+\phi_1)+\ddot{\phi}_2\sin(p\tau+\phi_2)\\
&\quad+(p+\dot{\phi}_1)^2\cos(p\tau+\phi_1)+(p+\dot{\phi}_2)^2\cos(p\tau+\phi_2)\},\\
\ddot{y}+p^2y&=\varepsilon\{-\xi_2y^3-\zeta\dot{y}+\sigma y+\alpha p^2[\lambda_1\sin p\tau+\lambda_2\sin(p\tau+\beta)]\\
&\quad+2\varepsilon^2\lambda_1p^2\sin p\tau-\ddot{\phi}_1\sin(p\tau+\phi_1)-\ddot{\phi}_2\sin(p\tau+\phi_2)\\
&\quad+(p+\dot{\phi}_1)^2\sin(p\tau+\phi_1)+(p+\dot{\phi}_2)^2\sin(p\tau+\phi_2)\},\\
\ddot{\phi}_1&=\varepsilon\mu\{(\ddot{x}-\varepsilon\lambda_1p^2\cos p\tau)\sin(p\tau+\phi_1)\\
&\quad-(\ddot{y}-\varepsilon\lambda_1p^2\sin p\tau)\cos(p\tau+\phi_1)-\zeta_1\dot{\phi}-\zeta_0[(p+\dot{\phi}_1)^2\\
&\quad-\varepsilon(\ddot{x}-\varepsilon\lambda_1p^2\cos p\tau)\cos(p\tau+\phi_1)\\
&\quad-\varepsilon(\ddot{y}-\varepsilon\lambda_1p^2\sin p\tau)\sin(p\tau+\phi_1)]\mathrm{sign}(\dot{\phi}_1)\},\\
\ddot{\phi}_2&=\varepsilon\mu\{(\ddot{x}-\varepsilon\lambda_1p^2\cos p\tau)\sin(p\tau+\phi_2)\\
&\quad-(\ddot{y}-\varepsilon\lambda_1p^2\sin p\tau)\cos(p\tau+\phi_2)-\zeta_1\dot{\phi}-\zeta_0[(p+\dot{\phi}_2)^2\\
&\quad-\varepsilon(\ddot{x}-\varepsilon\lambda_1p^2\cos p\tau)\cos(p\tau+\phi_2)\\
&\quad-\varepsilon(\ddot{y}-\varepsilon\lambda_1p^2\sin p\tau)\sin(p\tau+\phi_2)]\mathrm{sign}(\dot{\phi}_2)\}.
\end{aligned}\tag{5}$$

From this point, the case with a pair of balls in an ABB is considered in this study because it is the simplest structure of an ABB capable of reducing a wide range of inherent imbalances using the disc–rotor system. The equations of motion in (5) are ready for a multiple-scale analysis, which begins with the following expansion of the dynamic variables:

$$\begin{aligned}
x(\tau;\varepsilon)&=x_0(T_0,T_1)+\varepsilon x_1(T_0,T_1)+O(\varepsilon^2),\\
y(\tau;\varepsilon)&=y_0(T_0,T_1)+\varepsilon y_1(T_0,T_1)+O(\varepsilon^2),\\
\phi_1(\tau;\varepsilon)&=\phi_{10}(T_0,T_1)+\varepsilon\phi_{11}(T_0,T_1)+O(\varepsilon^2),\\
\phi_2(\tau;\varepsilon)&=\phi_{20}(T_0,T_1)+\varepsilon\phi_{21}(T_0,T_1)+O(\varepsilon^2),
\end{aligned}\tag{6}$$

where $T_0=\tau$ is the fast time scale and $T_1=\varepsilon\tau$ is the slow time scale. The definitions of T_0 and T_1 yield

$$\frac{d}{d\tau}=D_0+\varepsilon D_1+O(\varepsilon^2),\quad \frac{d^2}{d\tau^2}=D_0^2+2\varepsilon D_0D_1+O(\varepsilon^2),\tag{7}$$

where $D_n=\partial/\partial T_n$ for $n=0,1$. Incorporating Eqs. (6) and (7) into the scaled Eq. (5) of motion results in different orders of ε. Collecting all the terms in $O(\varepsilon^0)$ and $O(\varepsilon^1)$ leads to the equations

$$D_0^2x_0+p^2x_0=0,\quad D_0^2y_0+p^2y_0=0,\quad D_0^2\phi_{10}=0,\quad D_0^2\phi_{20}=0,\tag{8}$$

and

$$\begin{aligned}
D_0^2x_1+p^2x_1&=-2D_0D_1x_0-\zeta D_0x_0+\alpha p^2[\lambda_1\cos(pT_0)+\lambda_2\cos(pT_0+\beta)]\\
&\quad+\sigma x_0-\xi_2x_0^3+D_0^2\phi_{10}\sin(pT_0+\phi_{10})\\
&\quad+(p+D_0\phi_{10})^2\cos(pT_0+\phi_{10})+D_0^2\phi_{20}\sin(pT_0+\phi_{20})\\
&\quad+(p+D_0\phi_{20})^2\cos(pT_0+\phi_{20}),\\
D_0^2y_1+p^2y_1&=-2D_0D_1y_0-\zeta D_0y_0+\alpha p^2[\lambda_1\sin(pT_0)+\lambda_2\sin(pT_0+\beta)]\\
&\quad+\sigma y_0-\xi_2y_0^3-D_0^2\phi_{10}\cos(pT_0+\phi_{10})\\
&\quad+(p+D_0\phi_{10})^2\sin(pT_0+\phi_{10})-D_0^2\phi_{20}\cos(pT_0+\phi_{20})\\
&\quad+(p+D_0\phi_{20})^2\sin(pT_0+\phi_{20}),\\
D_0^2\phi_{11}&=-2D_0D_1\phi_{10}+\mu[D_0^2x_0\sin(pT_0+\phi_{10})-D_0^2y_0\cos(pT_0+\phi_{10})\\
&\quad-\zeta_1D_0\phi_{10}-\zeta_0sign(D_0\phi_{10})(p+D_0\phi_{10})^2],\\
D_0^2\phi_{21}&=-2D_0D_1\phi_{20}+\mu[D_0^2x_0\sin(pT_0+\phi_{20})-D_0^2y_0\cos(pT_0+\phi_{20})\\
&\quad-\zeta_1D_0\phi_{20}-\zeta_0sign(D_0\phi_{20})(p+D_0\phi_{20})^2].
\end{aligned}\tag{9}$$

The solutions of Eq. (8) is assumed to be in the form of

$$\begin{aligned}
x_0&=A_0(T_1)e^{ipT_0}+\overline{A}_0(T_1)e^{-ipT_0},\quad y_0=B_0(T_1)e^{ipT_0}+\overline{B}_0(T_1)e^{-ipT_0},\\
\phi_{10}&=\psi_{10}(T_1)T_0+\varphi_{10}(T_1),\quad \phi_{20}=\psi_{20}(T_1)T_0+\varphi_{20}(T_1),
\end{aligned}\tag{10}$$

where $\overline{A}_0$ and $\overline{B}_0$ denote the complex conjugates of A_0 and B_0. $\{A_0,B_0,\overline{A}_0,\overline{B}_0\}$ are unknown parameters during the $O(\varepsilon^0)$ analysis. Their values can be determined during the $O(\varepsilon^1)$ analysis by first substituting the solution forms in Eq. (10) into the $O(\varepsilon^1)$ equations (Eq. (9)), yielding a set of new $O(\varepsilon^1)$ equations

$$\begin{aligned}
D_0^2x_1+p^2x_1&=e^{ipT_0}\left[-2pi\frac{\partial A_0}{\partial T_1}-\zeta piA_0+\sigma A_0-3\xi_2A_0^2\overline{A}_0+\frac{\alpha p^2\lambda_1}{2}\right.\\
&\quad\left.+\frac{\alpha p^2\lambda_2e^{i\beta}}{2}+\frac{(p+\psi_{10})^2e^{i\phi_{10}}}{2}+\frac{(p+\psi_{20})^2e^{i\phi_{20}}}{2}\right]\\
&\quad+e^{-ipT_0}\left[2pi\frac{\partial\overline{A_0}}{\partial T_1}+\zeta pi\overline{A}_0+\sigma\overline{A}_0-3\xi_2A_0\overline{A}_0^2+\frac{\alpha p^2\lambda_1}{2}\right.\\
&\quad\left.+\frac{\alpha p^2\lambda_2e^{-i\beta}}{2}+\frac{(p+\psi_{10})^2e^{-i\phi_{10}}}{2}+\frac{(p+\psi_{20})^2e^{-i\phi_{20}}}{2}\right],\\
D_0^2y_1+p^2y_1&=e^{ipT_0}\left[-2pi\frac{\partial B_0}{\partial T_1}-\zeta piB_0+\sigma B_0-3\xi_2B_0^2\overline{B}_0-\frac{i\alpha p^2\lambda_1}{2}\right.\\
&\quad\left.-\frac{i\alpha p^2\lambda_2e^{i\beta}}{2}-\frac{i(p+\psi_{10})^2e^{i\phi_{10}}}{2}-\frac{i(p+\psi_{20})^2e^{i\phi_{20}}}{2}\right]\\
&\quad+e^{-ipT_0}\left[2pi\frac{\partial\overline{B}_0}{\partial T_1}+\zeta pi\overline{B}_0+\sigma\overline{B}_0-3\xi_2B_0\overline{B}_0^2+\frac{i\alpha p^2\lambda_1}{2}\right.\\
&\quad\left.+\frac{i\alpha p^2\lambda_2e^{-i\beta}}{2}+\frac{i(p+\psi_{10})^2e^{-i\phi_{10}}}{2}+\frac{i(p+\psi_{20})^2e^{-i\phi_{20}}}{2}\right]\\
D_0^2\phi_{11}&=e^{i(2pT_0+\phi_{10})}\left[\frac{\mu p^2(iA_0+B_0)}{2}\right]+e^{-i(2pT_0+\phi_{10})}\left[\frac{\mu p^2(-i\overline{A}_0+\overline{B}_0)}{2}\right]\\
&\quad+\left\{-2\frac{\partial\psi_{10}}{\partial T_1}+e^{-i\phi_{10}}\left[\frac{\mu p^2(-iA_0+B_0)}{2}\right]+\mu\left[-\zeta_1\psi_{10}\right.\right.\\
&\quad\left.\left.-\zeta_0(p+\psi_{10})^2\mathrm{sgn}(\psi_{10})\right]\right\},\\
D_0^2\phi_{21}&=e^{i(2pT_0+\phi_{20})}\left[\frac{\mu p^2(iA_0+B_0)}{2}\right]+e^{-i(2pT_0+\phi_{20})}\left[\frac{\mu p^2(-i\overline{A}_0+\overline{B}_0)}{2}\right]\\
&\quad+\left\{-2\frac{\partial\psi_{20}}{\partial T_1}+e^{-i\phi_{20}}\left[\frac{\mu p^2(-iA_0+B_0)}{2}\right]+e^{i\phi_{10}}\left[\frac{\mu p^2(i\overline{A}_0+\overline{B}_0)}{2}\right]\right.\\
&\quad\left.+e^{i\phi_{20}}\left[\frac{\mu p^2(i\overline{A}_0+\overline{B}_0)}{2}\right]+\mu\left[-\zeta_1\psi_{20}-\zeta_0(p+\psi_{20})^2\mathrm{sgn}(\psi_{20})\right]\right\}.
\end{aligned}\tag{11}$$

The solutions of Eq. (11) x_1, y_1, ϕ_{11}, and ϕ_{21} can be found as follows:

$$x_1=A_1(T_1)e^{ipT_0}+\overline{A}_1(T_1)e^{-ipT_0}+\frac{1}{2ip}\left[A_{11}(T_1)T_0e^{ipT_0}-\overline{A}_{11}(T_1)T_0e^{-ipT_0}\right],$$

$$y_1 = B_1(T_1)e^{ipT_0} + \overline{B}_1(T_1)e^{-ipT_0} + \frac{1}{2ip}\left[B_{11}(T_1)T_0e^{ipT_0} - \overline{B}_{11}(T_1)T_0e^{-ipT_0}\right],$$

$$\phi_{11} = \frac{e^{i(2pT_0+\phi_{10})}}{-(2p+\psi_{10})^2}\left[\frac{\mu p^2(iA_0+B_0)}{2}\right] + \frac{e^{-i(2pT_0+\phi_{10})}}{-(2p+\psi_{10})^2}\left[\frac{\mu p^2(-i\overline{A}_0+\overline{B}_0)}{2}\right] + \left\{-2\frac{\partial\psi_{10}}{\partial T_1} + e^{-i\phi_{10}}\left[\frac{\mu p^2(-iA_0+B_0)}{2}\right] + e^{i\phi_{10}}\left[\frac{\mu p^2(i\overline{A}_0+\overline{B}_0)}{2}\right] + \mu[-\zeta_1\psi_{10} - \zeta_0(p+\psi_{10})^2\mathrm{sgn}(\psi_{10})]\right\}\frac{T_0^2}{2},$$

$$\phi_{21} = \frac{e^{i(2pT_0+\phi_{20})}}{-(2p+\psi_{20})^2}\left[\frac{\mu p^2(iA_0+B_0)}{2}\right] + \frac{e^{-i(2pT_0+\phi_{20})}}{-(2p+\psi_{20})^2}\left[\frac{\mu p^2(-i\overline{A}_0+\overline{B}_0)}{2}\right] + \left\{-2\frac{\partial\psi_{20}}{\partial T_1} + e^{-i\phi_{20}}\left[\frac{\mu p^2(-iA_0+B_0)}{2}\right] + e^{i\phi_{20}}\left[\frac{\mu p^2(i\overline{A}_0+\overline{B}_0)}{2}\right] + \mu\left[-\zeta_1\psi_{20} - \zeta_0(p+\psi_{20})^2\mathrm{sgn}(\psi_{20})\right]\right\}\frac{T_0^2}{2}. \quad (12)$$

Because T_0 is the fast scale, and T_1 is the slow scale, the coefficients of the T_0 and T_0^2 terms are zero. If the coefficients are not equal to zero, x_1, y_1, ϕ_{11}, and ϕ_{21}will be infinity. Next, we have

$$A_{11} = \left[-2pi\frac{\partial A_0}{\partial T_1} - \zeta piA_0 + \sigma A_0 - 3\xi_2 A_0^2\overline{A}_0 + \frac{\alpha p^2\lambda_1}{2} + \frac{\alpha p^2\lambda_2 e^{i\beta}}{2} + \frac{(p+\psi_{10})^2e^{i\phi_{10}}}{2} + \frac{(p+\psi_{20})^2e^{i\phi_{20}}}{2}\right] = 0,$$

$$B_{11} = \left[-2pi\frac{\partial B_0}{\partial T_1} - \zeta piB_0 + \sigma B_0 - 3\xi_2 B_0^2\overline{B}_0 - \frac{i\alpha p^2\lambda_1}{2} - \frac{i\alpha p^2\lambda_2 e^{i\beta}}{2} - \frac{i(p+\psi_{10})^2e^{i\phi_{10}}}{2} - \frac{i(p+\psi_{20})^2e^{i\phi_{20}}}{2}\right] = 0,$$

$$\left\{-2\frac{\partial\psi_{10}}{\partial T_1} + e^{-i\phi_{10}}\left[\frac{\mu p^2(-iA_0+B_0)}{2}\right] + e^{i\phi_{10}}\left[\frac{\mu p^2(i\overline{A}_0+\overline{B}_0)}{2}\right] + \mu[-\zeta_1\psi_{10} - \zeta_0(p+\psi_{10})^2\,\mathrm{sgn}(\psi_{10})]\right\} = 0,$$

$$\left\{-2\frac{\partial\psi_{20}}{\partial T_1} + e^{-i\phi_{20}}\left[\frac{\mu p^2(-iA_0+B_0)}{2}\right] + e^{i\phi_{20}}\left[\frac{\mu p^2(i\overline{A}_0+\overline{B}_0)}{2}\right] + \mu[-\zeta_1\psi_{20} - \zeta_0(p+\psi_{20})^2\mathrm{sgn}(\psi_{20})]\right\} = 0. \quad (13)$$

Note that the exponential forms in Eq. (11) are used for decomposing trigonometric functions for the convenience of the ensuing computations. The removal of the secular terms of Eq. (11) leads to four conditions. Incorporating formulations of A_0,$\overline{A}_0$,B_0, and $\overline{B}_0$ with real and imaginary parts

$$A_0 = a(T_1) + ib(T_1), \quad \overline{A}_0 = a(T_1) - ib(T_1),$$
$$B_0 = c(T_1) + id(T_1), \quad \overline{B}_0 = c(T_1) - id(T_1), \quad (14)$$

into the four secular-term-removal conditions leads to

$$\frac{\partial a}{\partial\tau} = \frac{\varepsilon}{2p}\left[-\zeta pa + \sigma b - 3\xi_2(a^2b + b^3) + \frac{\alpha\lambda_2 p^2}{2}\sin\beta + \frac{(p+\psi_{10})^2}{2}\sin\phi_{10} + \frac{(p+\psi_{20})^2}{2}\sin\phi_{20}\right],$$

$$\frac{\partial b}{\partial\tau} = -\frac{\varepsilon}{2p}\left[\zeta pb + \sigma a - 3\xi_2(a^3 + ab^2) + \frac{\alpha\lambda_1 p^2}{2} + \frac{\alpha\lambda_2 p^2}{2}\cos\beta + \frac{(p+\psi_{10})^2}{2}\cos\phi_{10} + \frac{(p+\psi_{20})^2}{2}\cos\phi_{20}\right],$$

$$\frac{\partial c}{\partial\tau} = \frac{\varepsilon}{2p}\left[-\zeta pc + \sigma d - 3\xi_2(c^2d + d^3) - \frac{\alpha\lambda_1 p^2}{2} - \frac{\alpha\lambda_2 p^2}{2}\cos\beta - \frac{(p+\psi_{10})^2}{2}\cos\phi_{10} - \frac{(p+\psi_{20})^2}{2}\cos\phi_{20}\right],$$

$$\frac{\partial d}{\partial\tau} = -\frac{\varepsilon}{2p}\left[\zeta pd + \sigma c - 3\xi_2(c^3 + cd^2) + \frac{\alpha\lambda_2 p^2}{2}\sin\beta + \frac{(p+\psi_{10})^2}{2}\sin\phi_{10} + \frac{(p+\psi_{20})^2}{2}\sin\phi_{20}\right],$$

$$\frac{\partial\psi_{10}}{\partial\tau} = \frac{\varepsilon\mu}{2}\left\{-\zeta_1\psi_{10} - \zeta_0\,sign(\psi_{10})(p+\psi_{10})^2 + p^2[(b+c)\cos\phi_{10} + (-a+d)\sin\phi_{10}]\right\},$$

$$\frac{\partial\psi_{20}}{\partial\tau} = \frac{\varepsilon\mu}{2}\left\{-\zeta_1\psi_{20} - \zeta_0\,sign(\psi_{20})(p+\psi_{20})^2 + p^2[(b+c)\cos\phi_{20} + (-a+d)\sin\phi_{20}]\right\},$$

$$\frac{\partial\phi_{10}}{\partial\tau} = \psi_{10},$$

$$\frac{\partial\phi_{20}}{\partial\tau} = \psi_{20}. \quad (15)$$

where $\{a, b, c, d\}$ are the real and imaginary parts of $\{A_0, B_0, \overline{A}_0, \overline{B}_0\}$, respectively.

For the purpose of obtaining the steady-state solutions, to attain

$$\sqrt{a_s^2 + b_s^2}\sin(\phi_{s10} - \upsilon) = 0, \sqrt{a_s^2 + b_s^2}\sin(\phi_{s20} - \upsilon) = 0. \quad (16)$$

Various steady-state solutions and the stability of the slow dynamic equation of the system (Eq. 15) were sought to predict the balancing ball positions and residual vibrations and to evaluate the performance of the balancer system.

Setting Eq. (15) equal to zero and acknowledging that $\psi_{S10} = \psi_{S20} = 0$, i.e., the balls are motionless at steady state, we obtain four types of different solutions based on the parameters of rotating speed, inherent rotating imbalance, and counter balance, which are shown in Fig. 3. The solutions surrounded with dash lines are stable, and the detailed derivations will be discussed in the following sections.

3.1. Type I solutions

There exist trivial solutions for the motion of suspension, i.e., $a_s = b_s = c_s = d_s = 0$. The corresponding ball positions can easily be found by numerically solving

$$\sin\phi_{S10} + \sin\phi_{S20} = -\alpha\lambda_2\sin\beta,$$
$$\cos\phi_{S10} + \cos\phi_{S20} = -\alpha\lambda_1 - \alpha\lambda_2\cos\beta, \quad (17)$$

which leads to

$$\sin^2(\phi_{S10} - \phi_{S20}) = 1 - \left[\frac{\alpha^2(\lambda_1^2 + \lambda_2^2)}{2} + \alpha^2\lambda_1\lambda_2\cos\beta - 1\right]^2.$$

Based on the form of Eq. (16), two balls stick together below the natural frequency of the suspension and diverge to distinct positions above the natural frequency at the steady state. For this type of solution, because $a_s = b_s = c_s = d_s = 0$; the system exhibits almost no residual vibrations, and this solution is the desired solution to minimize radial vibrations.

3.2. Type II solutions

There exist two different types of solutions that possess identical ball angular positions at the steady state. The first type of solution can easily be found by numerically solving

$$a_S = -d_S, b_S = c_S, \sin\upsilon = b_S/\sqrt{a_S^2 + b_S^2}, \cos\upsilon = a_S/\sqrt{a_S^2 + b_S^2},$$

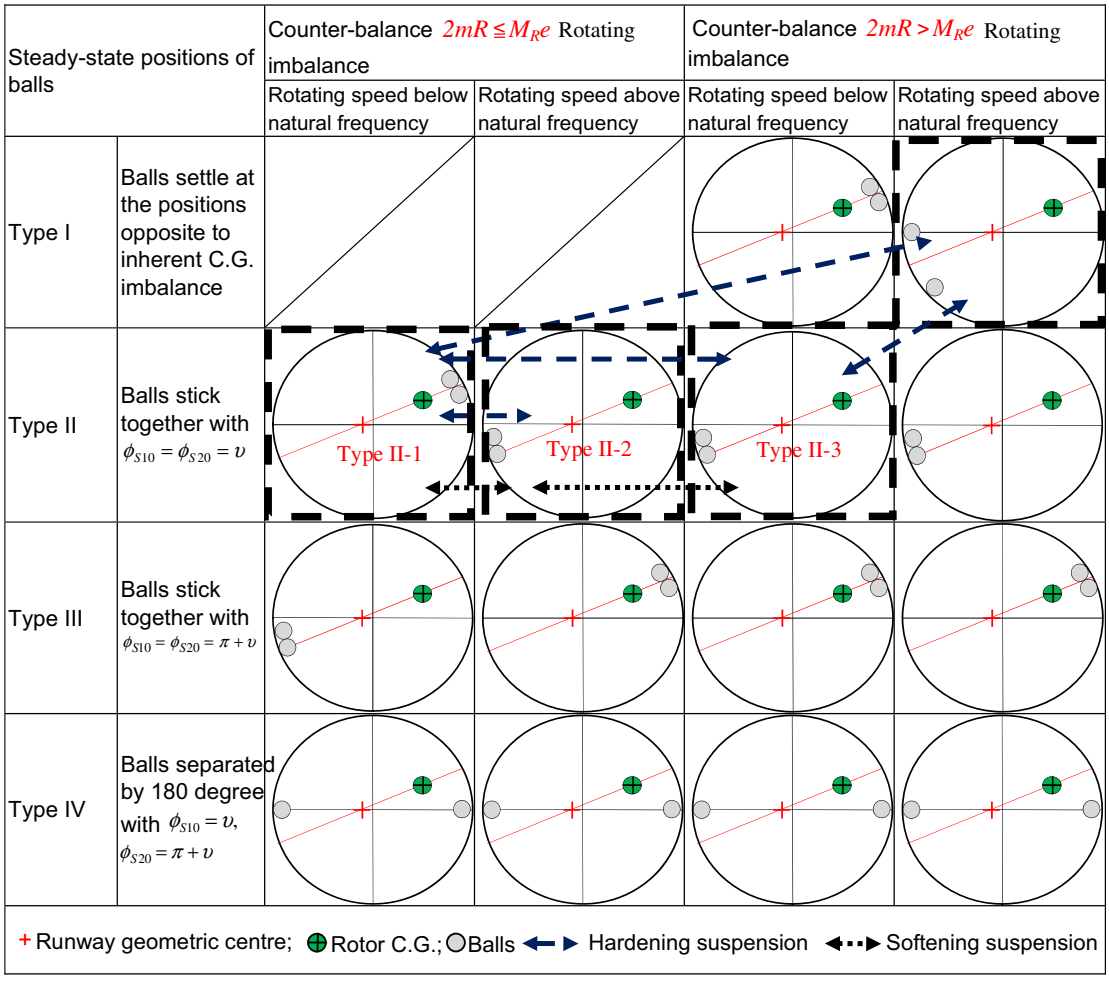

Fig. 3. Illustration of four types of steady-state positions for a pair of balancing balls.

$$-\zeta p a_S + \sigma b_S - 3\xi_2(a_s^2 b_S + b_S^3) + \frac{\alpha p^2 \lambda_2 \sin\beta}{2} + p^2 \sin\upsilon = 0,$$

$$\zeta p b_S + \sigma a_S - 3\xi_2(a_s^3 + a_S b_S^2) + \frac{\alpha p^2 \lambda_1}{2} + \frac{\alpha p^2 \lambda_2 \cos\beta}{2} + p^2 \cos\upsilon = 0,$$

$$\phi_{S10} = \phi_{S20} = 0.$$

where υ has two distinct solutions, denoted by υ_1 and υ_2, which lead to two solution sets containing the different steady states of ϕ_{S10}, ϕ_{S20}, a_S, and b_S.

3.3. Type III solutions

In this solution υ also has two distinct solutions, denoted by υ_1 and υ_2, which lead to two solution sets containing different steady states for ϕ_{S10}, ϕ_{S20}, a_S, and b_S. The steady-state dynamics with the Type II and Type III solutions are identical to the case with a single ball-type balancer system that reaches favourable balancing only if the total mass of the balancing balls is sized almost perfectly. In other words, the counterbalancing generated by the balls is almost equal to that by C.G. eccentricity, which is difficult to achieve because of manufacturing tolerance.

3.4. Type IV solutions

The Type IV solutions generate no counterbalance because of an exact mutual cancellation of the two counterbalancing forces generated by the two balls at steady state. Then, we use the perturbation methods to linearise Eq. (15) and assume that each solution a, b, c, d, ϕ_{10}, ϕ_{20}, ψ_{10}, and ψ_{20} has a small perturbation value of Δa, Δb, Δc, Δd, $\Delta\phi_1$, $\Delta\phi_2$, $\Delta\psi_1$, and $\Delta\psi_2$. Substituting each solution and small perturbation value into Eq. (15) yields the perturbation equations.

$$\Delta\dot{a} = \frac{\varepsilon}{2p}\left[-\zeta p\Delta a - 6\xi_2 a_s b_s \Delta a + \sigma\Delta b - 3\xi_2(a_s^2\Delta b + 3b_s^2\Delta b) + p\sin\phi_{S10}\Delta\psi_1 + p\sin\phi_{S20}\Delta\psi_2 + \frac{p^2\cos\phi_{S10}\Delta\phi_1}{2} + \frac{p^2\cos\phi_{S20}\Delta\phi_2}{2}\right],$$

$$\Delta\dot{b} = \frac{-\varepsilon}{2p}\left[\sigma\Delta a - 3\xi_2(3a_s^2\Delta a + b_s^2\Delta a) + \zeta p\Delta b - 6\xi_2 a_s b_s\Delta b + p\cos\phi_{S10}\Delta\psi_1 + p\cos\phi_{S20}\Delta\psi_2 - \frac{p^2\sin\phi_{S10}\Delta\phi_1}{2} - \frac{p^2\sin\phi_{S20}\Delta\phi_2}{2}\right],$$

$$\Delta\dot{c} = \frac{\varepsilon}{2p}\left[-\zeta p\Delta c - 6\xi_2 c_s d_s\Delta c + \sigma\Delta d - 3\xi_2(c_s^2\Delta d + 3d_s^2\Delta d) - p\cos\phi_{S10}\Delta\psi_1 - p\cos\phi_{S20}\Delta\psi_2 + \frac{p^2\sin\phi_{S10}\Delta\phi_1}{2} + \frac{p^2\sin\phi_{S20}\Delta\phi_2}{2}\right],$$

$$\Delta\dot{d} = \frac{-\varepsilon}{2p}\left[\sigma\Delta c - 3\xi_2(3c_s^2\Delta c + d_s^2\Delta d) + \zeta p\Delta d - 6\xi_2 c_s d_s\Delta d + p\sin\phi_{S10}\Delta\psi_1 + p\sin\phi_{S20}\Delta\psi_2 + \frac{p^2\cos\phi_{S10}\Delta\phi_1}{2} + \frac{p^2\cos\phi_{S20}\Delta\phi_2}{2}\right],$$

$$\Delta\dot{\psi}_1 = \varepsilon\left\{\frac{\mu p^2}{2}\left[-\Delta a\sin\phi_{S10} + \Delta b\cos\phi_{S10} - \Delta c\cos\phi_{S10} + \Delta d\sin\phi_{S10} - (b_s + c_s)\sin\phi_{s10}\Delta\phi_1 + (d_s - a_s)\cos\phi_{s10}\Delta\phi_1\right] - \frac{\mu\zeta_1}{2}\Delta\psi_1 - \mu\zeta_0 p\Delta\psi_1\right\},$$

$$\Delta\dot{\psi}_2 = \varepsilon\left\{\frac{\mu p^2}{2}\left[-\Delta a\sin\phi_{S20}+\Delta b\cos\phi_{S20}-\Delta c\cos\phi_{S20}+\Delta d\sin\phi_{S20} -(b_s+c_s)\sin\phi_{s20}\Delta\phi_2+(d_s-a_s)\cos\phi_{s20}\Delta\phi_2\right]-\frac{\mu\zeta_1}{2}\Delta\psi_2-\mu\zeta_0 p\Delta\psi_2\right\},$$

$$\Delta\dot{\phi}_1 = \Delta\psi_1,$$
$$\Delta\dot{\phi}_2 = \Delta\psi_2. \tag{18}$$

Then, we can determine the stability of each steady-state solution on the basis of Eq. (18). If the solution converges to zero, we can assume that the steady-state solution is true. Eq. (18) represents a set of first-order differential equations, and thus we can rewrite it in a matrix form

$$\Delta\dot{\underline{X}}(\tau) = A_x\Delta\underline{X}(\tau), \tag{19}$$

Then, we find matrix A_x as follows:

$$A_x = \begin{bmatrix} N_1 & 0 & N_5 & N_8 \\ 0 & N_2 & N_6 & N_9 \\ 0 & 0 & 0 & N_{10} \\ N_3 & N_4 & N_7 & N_{11} \end{bmatrix}$$

and

$$[N_1] = \begin{bmatrix} -\frac{\varepsilon\zeta}{2}-\frac{3\varepsilon\xi_2 a_s b_s}{P} & \frac{\varepsilon\sigma}{2p}-\frac{3\varepsilon\xi_2(a_s^2+3b_s^2)}{2p} \\ -\frac{\varepsilon\sigma}{2p}+\frac{3\varepsilon\xi_2(3a_s^2+b_s^2)}{2p} & -\frac{\varepsilon\zeta}{2}+\frac{3\varepsilon\xi_2 a_s b_s}{P} \end{bmatrix},$$

$$[N_2] = \begin{bmatrix} -\frac{\varepsilon\zeta}{2}-\frac{3\varepsilon\xi_2 c_s d_s}{P} & \frac{\varepsilon\sigma}{2p}-\frac{3\varepsilon\xi_2(3c_s^2+d_s^2)}{2P} \\ -\frac{\varepsilon\sigma}{2p}+\frac{3\varepsilon\xi_2(3c_s^2+d_s^2)}{2P} & -\frac{\varepsilon\zeta}{2}+\frac{3\varepsilon\xi_2 c_s d_s}{P} \end{bmatrix},$$

$$[N_3] = \begin{bmatrix} -\frac{\varepsilon\mu p^2}{2}\sin\phi_{S10} & \frac{\varepsilon\mu p^2}{2}\cos\phi_{S10} \\ -\frac{\varepsilon\mu p^2}{2}\sin\phi_{S20} & \frac{\varepsilon\mu p^2}{2}\cos\phi_{S20} \end{bmatrix},$$

$$[N_4] = \begin{bmatrix} \frac{\varepsilon\mu p^2}{2}\cos\phi_{S10} & \frac{\varepsilon\mu p^2}{2}\sin\phi_{S10} \\ \frac{\varepsilon\mu p^2}{2}\cos\phi_{S20} & \frac{\varepsilon\mu p^2}{2}\sin\phi_{S20} \end{bmatrix},$$

$$[N_5] = \begin{bmatrix} \frac{\varepsilon p}{4}\cos\phi_{S10} & \frac{\varepsilon p}{4}\cos\phi_{S20} \\ \frac{\varepsilon p}{4}\sin\phi_{S10} & \frac{\varepsilon p}{4}\sin\phi_{S20} \end{bmatrix},$$

$$[N_6] = \begin{bmatrix} \frac{\varepsilon p}{4}\sin\phi_{S10} & \frac{\varepsilon p}{4}\sin\phi_{S20} \\ -\frac{\varepsilon p}{4}\cos\phi_{S10} & -\frac{\varepsilon p}{4}\cos\phi_{S20} \end{bmatrix},$$

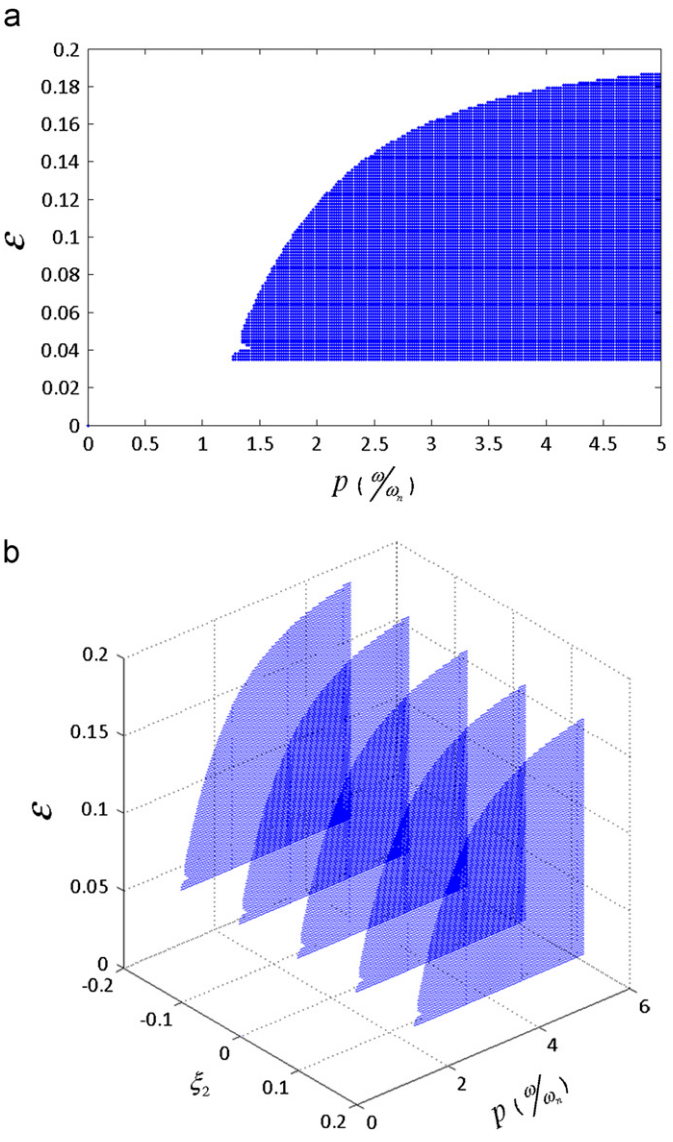

Fig. 4. Stability diagram of scaling parameter ε, speed ratio p and ξ_2 ($\xi_2=-0.2$, $\xi_2=-0.1$, $\xi_2=0$, $\xi_2=0.1$ and $\xi_2=0.2$) for Type I solutions.

Table 1
Values of system parameters.

Properties	Symbol	Values (unit)	Reference values from commercial optic drives
Natural frequency of the linear spring	ω_n	11.2 Hz	8–40 Hz
Mass of the equivalent stator	M_S	110 g	$M=M_s+M_R+nm$
Mass of the equivalent rotor	M_R	40 g	Total mass M : 100–150 g
Ball mass	m	0.2 g	Disc mass : around 15.8 g
Ball radius	r	1 mm	1.25 mm
Race radius	R	16.5 mm	15 mm
Equivalent suspension damping	C_X and C_Y	$C_X=C_Y\approx 2\zeta M\omega_n$	$C_X=C_Y\approx 2\zeta M\omega_n$
Damping ratio	ζ	0.025	0.1 for rubber
C.G. eccentricity	e	0.1 mm	0.05 for plastic
Race eccentricity	ρ	0.01 mm	0.025 for metal
Adhesive coefficient	α_1	$2\times10^{-5}\left(\mathrm{N}\frac{\mathrm{sec}}{\mathrm{m}^2}\right)$	Around 0.1 mm 0.001–0.05 mm $2\times10^{-5}\left(\mathrm{N}\frac{\mathrm{sec}}{\mathrm{m}^2}\right)$

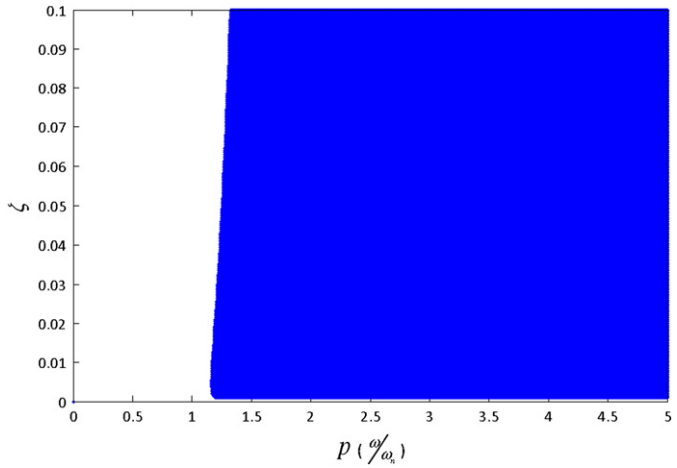

Fig. 5. Stability diagram of damping ratio ζ versus speed ratio p for Type I solutions.

$$[N_7] = \begin{bmatrix} \frac{\varepsilon\mu p^2}{2}(-(b_s+c_s)\sin\phi_{s10}+(d_s-a_s)\cos\phi_{s10}) & 0 \\ 0 & \frac{\varepsilon\mu p^2}{2}(-(b_s+c_s)\sin\phi_{s20}+(d_s-a_s)\cos\phi_{s20}) \end{bmatrix},$$

$$[N_8] = \begin{bmatrix} \frac{\varepsilon}{2}\sin\phi_{S10} & \frac{\varepsilon}{2}\sin\phi_{S20} \\ -\frac{\varepsilon}{2}\cos\phi_{S10} & -\frac{\varepsilon}{2}\cos\phi_{S20} \end{bmatrix},$$

$$[N_9] = \begin{bmatrix} -\frac{\varepsilon}{2}\cos\phi_{S10} & -\frac{\varepsilon}{2}\cos\phi_{S20} \\ -\frac{\varepsilon}{2}\sin\phi_{S10} & -\frac{\varepsilon}{2}\sin\phi_{S20} \end{bmatrix},$$

$$[N_{10}] = \begin{bmatrix} 1 & 0 \\ 0 & 1 \end{bmatrix}, \quad [N_{11}] = \begin{bmatrix} -\frac{\varepsilon\mu(\zeta_1+2\zeta_0 p)}{2} & 0 \\ 0 & -\frac{\varepsilon\mu(\zeta_1+2\zeta_0 p)}{2} \end{bmatrix},$$

$$\Delta X(\tau) = \begin{bmatrix} \Delta a & \Delta b & \Delta c & \Delta d & \Delta\phi_1 & \Delta\phi_2 & \Delta\psi_1 & \Delta\psi_2 \end{bmatrix}^{\mathrm{T}}.$$

If $\Delta\underline{X}(\tau) = e^{s\tau}$, then $[A_x - \underline{I}S]\Delta\underline{X}(\tau) = 0$. S is the eigenvalue, $[A_x - \underline{I}\,S] = 0$ is the perturbation characteristic equation, and $\underline{I}$ is a unit matrix. If the real parts of all eigenvalues are lower than zero, the system is stable. Otherwise, the system is unstable.

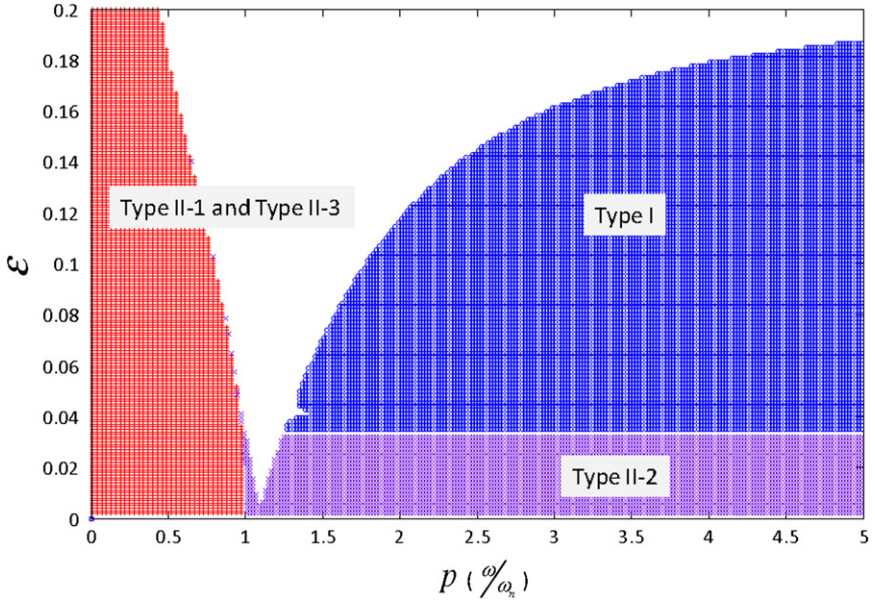

Fig. 6. Stability diagram of Type I and II solutions for a linear spring ($\xi_2 = 0$).

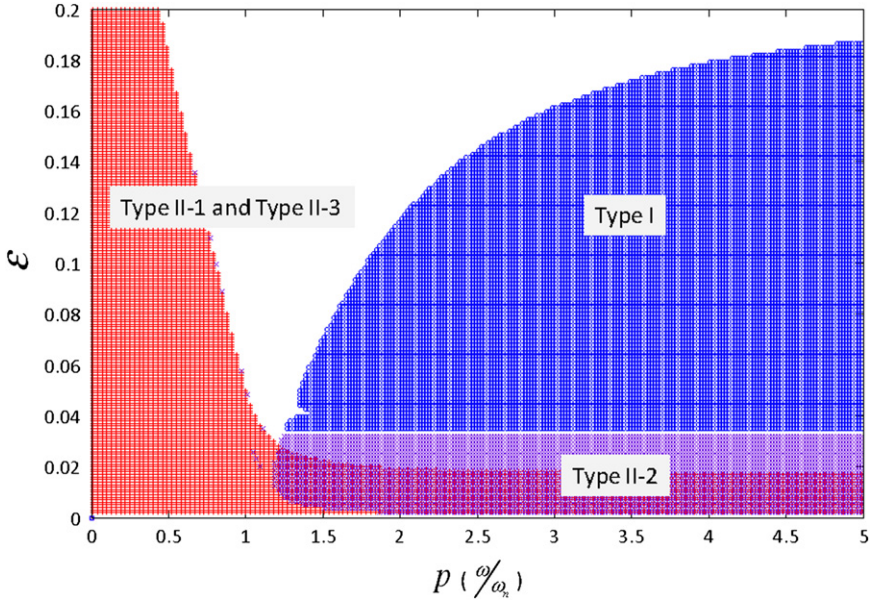

Fig. 7. Stability diagram of Type I and II solutions for a stiffness hardening spring ($\xi_2 = 0.2$).

4. Stability analysis

The parameters listed in Table 1 are related to optical disc drives manufactured by Lite-On IT Corporation, Taiwan. The values of the system parameters employed in this study. Fig. 4 shows the stability diagram for Type I solutions that, on the basis of the conclusion drawn in Fig. 4, render the best radial vibration reduction compared to the other solutions. To ensure the stability of the Type I solution, we need to design a balancing system such that (p,ε) falls within the dot-shaded region in Fig. 4(a). The Type I (perfectly balanced solutions) and their existence region cannot be modified by non-linearity in this paper because of $a_s = b_s = c_s = d_s = 0$; the system exhibits almost no residual vibrations, and this solution is the desired solution to minimize radial vibrations. We can see the results in Fig. 4(b). Type I solution cannot be modified by non-linearity ($\xi_2 = -0.2$, $\xi_2 = -0.1$, $\xi_2 = 0$, $\xi_2 = 0.1$, $\xi_2 = 0.2$).

This requires that three conditions related to the system parameters be satisfied. First, the system has to operate above the resonance frequency, i.e., $p > 1$. Second, the maximal counterbalance (two balls sticking together) has to be greater than the inherent imbalance, i.e., $2mR > M_R e$, which corresponds to the area $\varepsilon > 0.035$ in Fig. 4. Third, the total mass of the balls has to be sufficiently small for ε to not exceed a certain level to deteriorate stability, which corresponds to the curve prescribing the upper boundary of the dot-shaded region in Fig. 4. The stability diagram is not influenced by the non-linear characteristics of the suspension in the Type I solution because the residual vibration approaches zero. When the damping ratio (ζ) changes from 0.001 to 0.1, we find that the stability area in Fig. 5 varies with respect to the speed ratio.

Figs. 6–8, respectively, show the stabilities of steady-state solutions with different characteristics of the suspensions, i.e., linear, non-linear stiffness hardening and softening springs. We can observe that the stability diagrams are affected by the non-linear suspension near resonance frequency. The stiffness hardening spring ($\xi_2 = 0.2$) enlarges the stable region of Type II-1 and Type II-3 to the region with the high-speed ratio, as shown in Fig. 7, which is larger than that of the linear spring in Fig. 6. In addition, Fig. 7 also illustrates overlapped region consists of Type II-1, II-2, and II-3. However, if we increase stiffness hardening stiffness factor (ξ_2), the unwanted stability regions for Type II-1 and Type II-3 will overlapped to Type I region. The overlapped region will cause inconsistency in ball positioning to counteract the inherent imbalance. The non-linear softening spring ($\xi_2 = -0.2$) causes the stable region of Type II-2 to approach the region of the low speed ratio as shown in Fig. 8, which is also different from that of the linear spring, as shown in Fig. 6.

The increased stability region of the Type II-2 solution is affected by the non-linear stiffness softening spring and overlaps the Type II-1 solution in the region with a lower speed ratio. Therefore, one can observe that the balance behaviour still occurs even though the rotor speed is less than the natural frequency of the linear spring. In addition, the unwanted stability regions for Type II-1 and Type II-3 increase because of the stiffness hardening suspension but decrease due to the effect of the softening suspension, as shown in Figs. 7 and 8, respectively.

The analysis of the effect of the cubic coefficient is shown in Fig. 9. Simulation results are shown for a selection of xi (ξ_2) to verify the potential area where softening supports may extend the stability region of the balanced state to subcritical rotor speeds. From the results, we can see the trend of stability boundaries for a large section of xi (ξ_2). The non-linear softening spring ($\xi_2 = -0.4$, $\xi_2 = -0.3$,

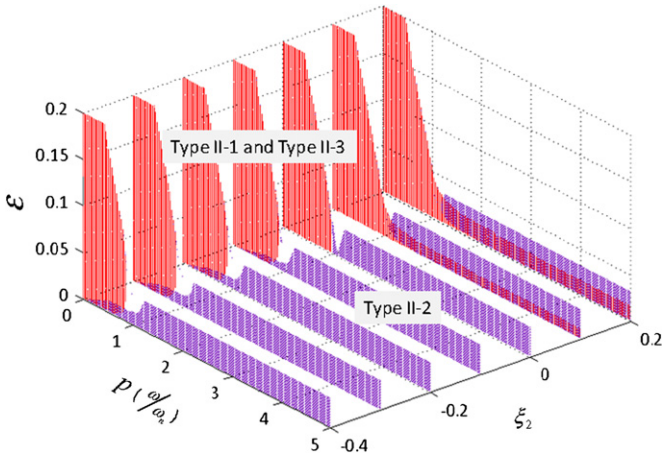

Fig. 9. Stability diagram of Type II solutions for large section of non-linear stiffness spring ($\xi_2 = -0.4$, $\xi_2 = -0.3$, $\xi_2 = -0.2$, $\xi_2 = -0.1$, $\xi_2 = 0$, $\xi_2 = 0.1$, and $\xi_2 = 0.2$).

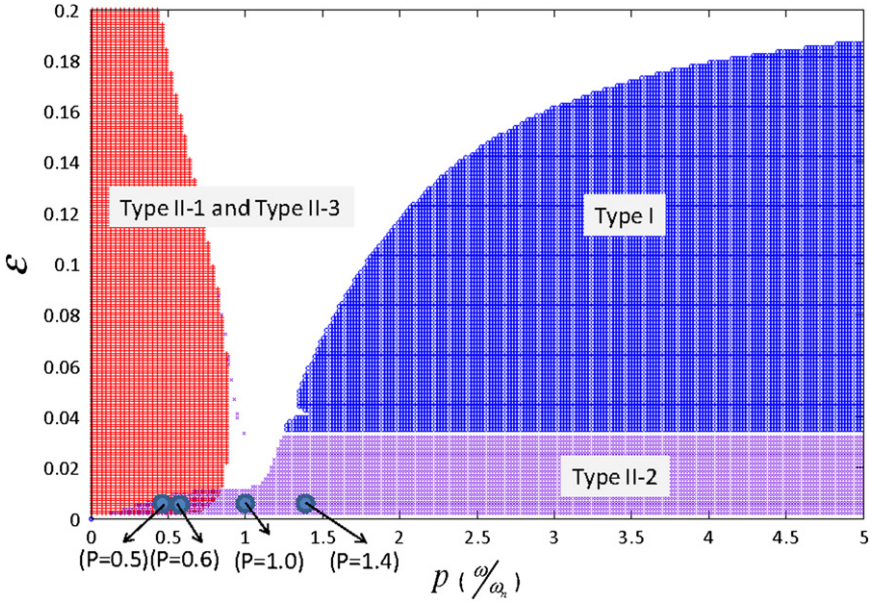

Fig. 8. Stability diagram of Type I and II solutions for a stiffness softening spring ($\xi_2 = -0.2$).

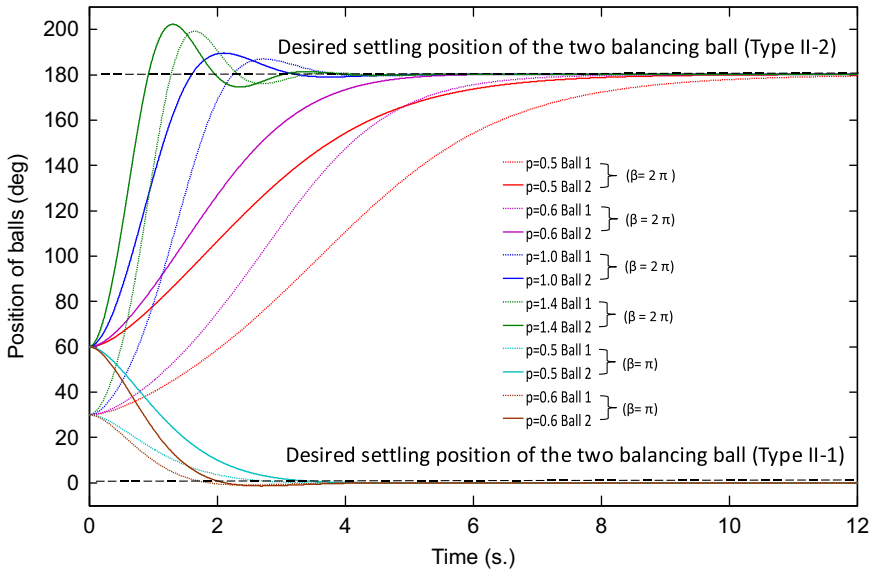

Fig. 10. Dynamic responses corresponding to points marked in Fig. 8. Initial conditions are fixed at $x=y=\dot{x}=\dot{y}=\dot{\phi}_1=\dot{\phi}_2=0$, $\phi_1=30^\circ$, $\phi_2=60^\circ$.

$\xi_2=-0.2$, $\xi_2=-0.1$) causes the stable regions of Type II-2 to approach the region of low speed ratio as shown in Fig. 9. The stiffness hardening spring ($\xi_2=0.2$, $\xi_2=0.1$) enlarges the stable regions of Type II-1 and Type II-3 to the region of high-speed ratio, as shown in Figs. 7 and 9. One ought to avoid design in the overlapped region because the bi-stable phenomena may cause uncertain balanced performance of the ABB system for applications.

The non-linear suspension via time domain simulations of the response results is shown in Fig. 10 to verify the balanced performance and the bi-stable phenomena due to the non-linear suspension. The black dashed lines denote the desired settling ball positions of Type II-1 and Type II-2 solutions, which render to raise the imbalance and counteract the inherent imbalance, respectively. The two balancing balls can shorten time to reach desired settling ball positions when increasing speed ratio (p). The overlapping stable regions indicate that the Type II-1 and Type II-2 regions coexist and are both stable. The phase angles of the Type II-1 solution is

$$\tan^{-1}\left(\zeta p\sqrt{a_s^2+b_s^2}\Big/\sqrt{a_s^2+b_s^2}\left(\tfrac{p^2-1}{\varepsilon}\right)-3\zeta_2\sqrt{a_s^2+b_s^2}^{\,3}+p^2\right)$$

and that of the Type II-2 solution is

$$\tan^{-1}\left(\zeta p\sqrt{a_s^2+b_s^2}\Big/\sqrt{a_s^2+b_s^2}\left(\tfrac{p^2-1}{\varepsilon}\right)-3\zeta_2\sqrt{a_s^2+b_s^2}^{\,3}+p^2\right)+\pi$$

Type II-1 will cause more residual vibration than Type II-2, because of desired settling position of the two balancing ball. However, the Type II-2 solution can counterbalance part of imbalanced mass, although it still cannot achieve perfect balance because of $2mR<M_Re$. The system converges to type II-2 solutions with two balancing balls settled at the same positions eliminate radial vibrations via the counterbalancing.

5. Conclusions

This study investigated the non-linear dynamic effects of the suspension on the performance of an ABB. The positions where the balls reside in the ABB in the case of a non-linear suspension were different than those in a linear suspension. The stability diagram of Type I solution is not influenced by the non-linear suspension because the residual vibration approaches zero. When the damping ratio (ζ) changes, we observe that the stability area changes with respect to the speed ratio.

We can also observe that the stability diagrams are affected by the non-linear characteristics of the suspension. In contract to the perfectly balanced (Type I) solutions, the other solution (Type II) solution is affected by non-linear stiffness suspension. The non-linear stiffness hardening spring results in a larger stable region for Type II-1 and II-3 solutions with an increasing speed ratio than that of the linear spring. On the other hand, the non-linear softening spring causes a smaller stable region in the neighbourhood of the natural frequency. The increased stability region of Type II-2 solution affected by the non-linear stiffness softening spring overlaps that of the Type II-1 solution. Hence, the balance behaviour still occurs even though the rotor speed is less than the natural frequency of the linear spring. In addition, the overlapped stable region will cause the inconsistency in ball positioning to counteract the inherent imbalance. The non-linear softening suspension is preferred over the non-linear hardening suspension for the design of an ABB.

Acknowledgements

The authors are greatly indebted to the National Science Council of the R.O.C. for supporting the research through contracts (Grant numbers 97-2221-E-007-050-MY3, NSC-96-2221-E-007-075). Dr. Chun-Lung Huang's comments have been very useful for our research.

References

[1] E.L. Thearle, Automatic dynamic balancers (Part 1–Leblanc Balancer), Machine Design 22 (1950) 119–124.
[2] E.L. Thearle, Automatic dynamic balancers (Part 2–Ring, Pendulum, Ball balancers), Machine Design 22 (1950) 103–106.
[3] T. Majewski, Position errors occurrence in self balancers used on rigid rotors of rotating machinery, Journal of Mechanism and Machine Theory 23 (1988) 71–78.
[4] C. Rajalingham, B.R. Bhat, S. Rakheja, Automatic balancing of flexible vertical rotors using a guided ball, International Journal of Mechanical Sciences 40 (9)(1998) 825–834.

[5] W.Y. Huang, C.P. Chao, J.R. Kang, C.K. Sung, The application of ball-type balancers for radial vibration reduction of high-speed optic disk drives, Journal of Sound and Vibration 250 (3)(2002) 415–430.
[6] C.J. Lu, C.H. Hung, Stability analysis of a three-ball automatic balancer, Journal of Vibration and Acoustics Transactions of the ASME 130/051008 (2008) 1–7.
[7] D.J. Rodrigues, A.R. Champneys, M.I. Friswell, R.E. Wilson, Automatic two-plane balancing for rigid rotors, International Journal of Non-Linear Mechanics 43 (2008) 527–541.
[8] H.A. DeSmidt, Imbalance vibration suppression of a supercritical shaft via an automatic balancing device, Journal of Vibration and Acoustics Transactions of the ASME 131/041001 (2009) 1–13.
[9] J. Liu, Y. Ishida, Vibration suppression of rotating machinery utilizing an automatic ball balancer and discontinuous spring characteristics, Journal of Vibration and Acoustics Transactions of the ASME 131/0410004 (2009) 1–7.
[10] J. Ehyaei, M.M. Moghaddam, Dynamic response and stability analysis of an unbalanced flexible rotating shaft equipped with n automatic ball-balancers, Journal of Sound and Vibration 321 (3–5)(2009) 554–571.
[11] K. Green, A.R. Champneys, N.J. Lieven, Bifurcation analysis of an automatic dynamic balancing mechanism for eccentric rotors, Journal of Sound and Vibration 291 (2006) 861–881.
[12] C.P. Chao, B.C. Yo, C.K. Sung, Non-linear dynamic effects of damping washers on the performance of automatic ball balancers in optical disc drives, International Journal of Nonlinear Sciences and Numerical Simulation 7 (3)(2006) 275–278.